Copyright © 1997, American Institute of Aeronautics and Astronautics, Inc.

Three Dimensional Droplet Trajectory Code for Propellers of Arbitrary Geometry

K.A. Farag* and M. B. Bragg+
University of Illinois at Urbana-Champaign

ABSTRACT

A three-dimensional droplet impingement code for aircraft propellers has been developed. The code allows the modeling of propellers of arbitrary geometry in three dimensions, but is limited to modeling axi-symmetric spinner / nacelles combinations. The code was used to analyze several 3-D wind tunnel propeller-nacelle models which were experimentally studied. The code was also used to validate a theoretical relationship between two-dimensional and three-dimensional impingement efficiencies for rotating propellers. The effects of the spinner, engine nacelle geometry, contraction of the slipstream, and blade-to-blade interference on the impingement efficiency and limits of impingement were studied. Parametric studies of the effects of the advance ratio J and droplet size on the efficiencies and limits were performed.

NOMENCLATURE

A_d	Droplet's cross-sectional Area.
$\vec{B}$	Buoyancy force vector.
C_D	Droplet drag coefficient.
C_l	Local lift coefficient.
d	droplet diameter.
$\vec{D}$	Drag force vector.
F_r	Froude number of the flow.
$\vec{G}$	Gravitational force vector.
g	Gravitational acceleration.
J	Advance ratio.
K	Droplet's inertia parameter.
K_0	Droplet's modified inertia parameter.
L	Characteristic length.
R_s	Slip velocity Reynolds Number
R_∞	Freestream Reynolds Number.
R	Propeller radius.
$\vec{r}$	Position vector.
τ	Non-dimensional time.
U_∞	Freestream velocity.
$\vec{U}$	Flow velocity vector.
$\vec{V}$	Droplet velocity vector.
$\vec{V}_{slip}$	Droplet slip velocity.
ξ	Non-dimensional x coordinate.
η	Non-dimensional y coordinate.
ζ	Non-dimensional z coordinate.
ω	Rotation rate.
ρ_d	Droplet's mass density.
ρ	Freestream mass density.
σ	Freestream to droplet mass density ratio.

INTRODUCTION

The increased demands for fuel efficiency has intensified the search for efficient propellers for commercial and general aviation aircraft. One aspect of the design of such propellers is the ability to predict their susceptibility to accrete ice when operating in icing conditions. Icing occurs on propeller blades when supercooled water droplets suspended in the atmosphere impinge on the rotating blades. The mass flux of liquid water striking the blades as well as the most aft locations of the impinging droplet trajectories, limits of impingement, are important parameters used in the design of propeller ice protection.

* PH.D. Candidate The Ohio State University, Columbus, Ohio, Visiting Scholar, University of Illinois at Urbana-Champaign, Member AIAA.

+ Professor, Department of Aeronautical and Astronautical Engineering, University of Illinois at Urbana-Champaign, Associate Fellow AIAA.

Copyright ©1998 by K. A. Farag, and M. B. Bragg. Published by the American Institute of Aeronautics and Astronautics, Inc. with permission.

Copyright © 1997, American Institute of Aeronautics and Astronautics, Inc.

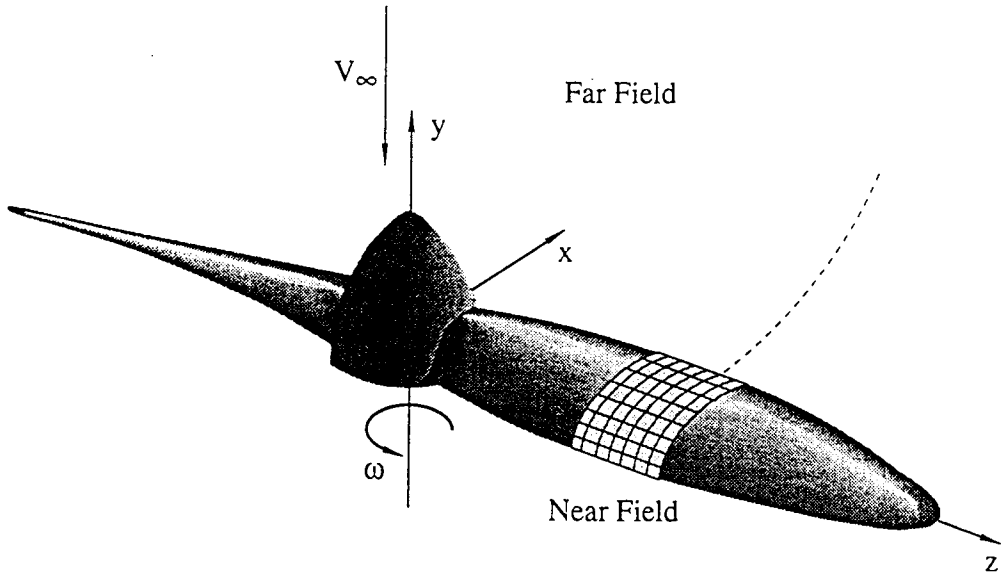

Fig. 1 The two-stage flow-field solutions used in the BETAPPROP code.

Virtually all previous efforts to computationally predict the impingement efficiency and limits of impingement of supercooled water droplets on propellers and rotor blades are based on the classical propeller strip analysis such as the work done by Korkan et al.[1, 2, 3, 4] Guffond et al.[5, 6] calculated the 3-D catch efficiency on a non-rotating helicopter rotor.

In such an approach, the propeller blade is divided into a finite number of strips; each of which is modeled as a two-dimensional airfoil. The flow field about each blade strip is computed separately and an iteration is performed on the total integrated inflow which is adjusted (by varying the induced angle of attack distribution) until agreement with the inflow value obtained from the classical momentum theory is achieved.

Once the distribution of the induced flow angle along the span of the propeller blade is found, the effective angle of attack of each blade section is determined. The flow field around each blade strip is then modeled as a two-dimensional airfoil operating at the effective angle of attack obtained from the above iteration. Droplet trajectories are then computed by integration of the droplet equations of motion utilizing the two-dimensional flow field for the propeller strips. The impingement limits and the impingement efficiency are calculated in the usual way. Two-dimensional strip analysis does neglect three-dimensional flow-field effects which may be important in the study of the icing characteristics of propeller blades.

In order to thoroughly understand the effects and significance of any three-dimensional effects on the icing characteristics of propeller blades, a three-dimensional droplet trajectory and impingement code was developed. The code has a versatile 3-D surface geometry generator capable of modeling arbitrary 3-D multiple-blade propellers with spinner. The code, however, is limited to modeling only axi-symmetric engine-nacelle combinations.

COMPUTATIONAL APPROACH

The code utilizes two separate three-dimensional potential flow solutions of the propeller-spinner and engine-nacelle assembly as shown in Fig. 1. The first is an optional far-field solution using vortex lattice methods (VLM). The use of this simplified model was intended to reduce the CPU time in the analysis of highly complex propeller geometries. Further, the VLM solution can be used to verify the convergence of the PM solution.

In the vortex lattice solution, the propeller blades are modeled as highly twisted thin surfaces lying on the mean-chamber lines of the airfoil sections along the span of the blade. A system of three-dimensional horseshoe vortices are used which are bound to the mean chamber surfaces with their trailing filaments convected downstream along a helix of constant pitch. The magnitude of the circulation associated with every horseshoe is determined by imposing flow tangency boundary conditions at a finite number of control points on the mean chamber surface.

Copyright © 1997, American Institute of Aeronautics and Astronautics, Inc.

The second flow-field method is based on a first-order panel method (PM). This solution can be used in the near-field in combination with the VLM in the far-field, or can be used alone for the entire flow field. In the PM solution, the three-dimensional geometry is modeled by a discrete array of 3-D rectangular panels tangent to the surface of the blade. It is further assumed that on every panel there exists a point source and a doublet of constant strength. The strength of the sources and doublets is obtained directly by requiring the resulting flow field to be tangent to the discretized surface at the geometric centeroids of the surface panels (Control Points). Figure 2 shows the geometry of the panels used in the VLM and PM solutions.

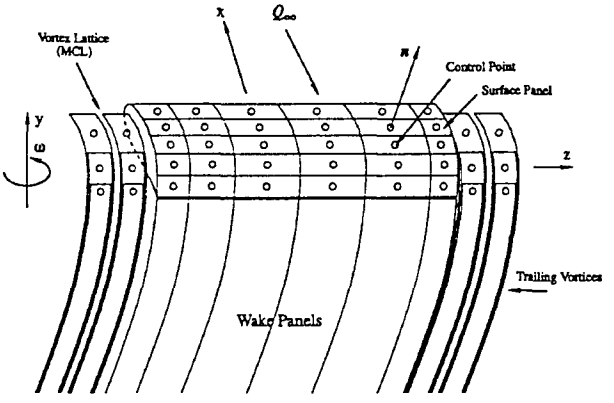

Fig. 2 The approximating geometry of the near and far-field surfaces

Panel methods fail to give accurate velocities at points within one-panel characteristic length measured from the sides of the panels. For that reason, a three-dimensional right rectangular grid is constructed off of the surface of the blade. The grid in Fig. 3 is constructed to cover only the panel corners that are later targeted and hit by calculated droplet trajectories. Accurate velocity values are assigned to the outer and inner edges of the surface grid. Linear interpolation is used to find the velocity anywhere inside the grid.

The three dimensional geometry of one of the propellers studied is shown in Fig. 4. The main blade was approximated by 16 radial panel columns. The propeller airfoil sections were approximated by 30 chordwise panels. Every radial panel column on which β calculations are desired, is further subdivided into five subpanel columns for the construction of the surface interpolation grid.

The equations of motion for a supercooled droplet suspended in the atmosphere were developed in a rotating reference frame to simplify the calculation. Buoyancy, gravitational and pressure gradient forces were neglected. The equations of motion are integrated in time assuming no initial relative motion with respect to the freestream. The resulting trajectories are examined for surface penetration. An iteration is performed on the droplets initial location until a trajectory piercing the surface is found. Four separate trajectories striking the four corners of the surface panels are found. The four impinging trajectories are assumed to bound the stream-tube of liquid striking the surface. The impingement efficiency is calculated as the ratio of mass striking the surface non-dimensionalized by the freestream mass flux at a given radial location.

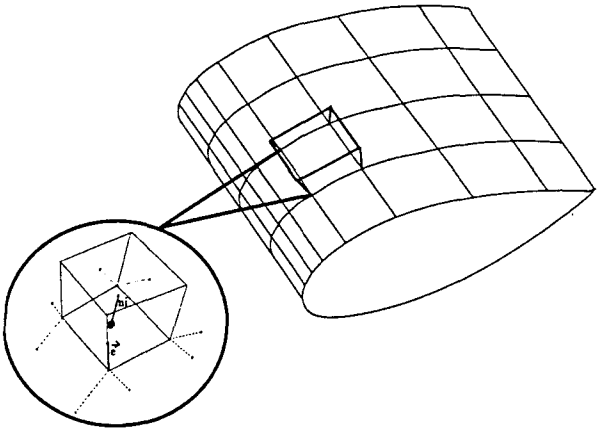

Fig. 3 The surface interpolation grid.

Aerodynamic Model

The BETAPROP code used in this analysis utilizes two separate flow field models to calculate the potential flow. A vortex lattice potential flow solver in the far-field region (one propeller diameter upstream from the plane of rotation). Closer to the plane of rotation and near the surface of the blade, the code utilizes a first order panel method potential flow solution. The panel solution is obtained from a version of PMARC[7] after undergoing substantial alteration and adaptation to rotating reference frames. PMARC is a first order panel code that is capable of modeling external and internal incompressible potential flow.

The PM part of the code uses a constant source and doublet distributions on flat rectangular pan-

Copyright © 1997, American Institute of Aeronautics and Astronautics, Inc.

els that are used to approximate the propeller and nacelle surface in question. The PM module in the code has an additional option where panels distant from the point where the local velocity is desired; in the far field, are approximated as point source and point doublets. The use of this option causes significant computational time savings with reasonable accuracy.

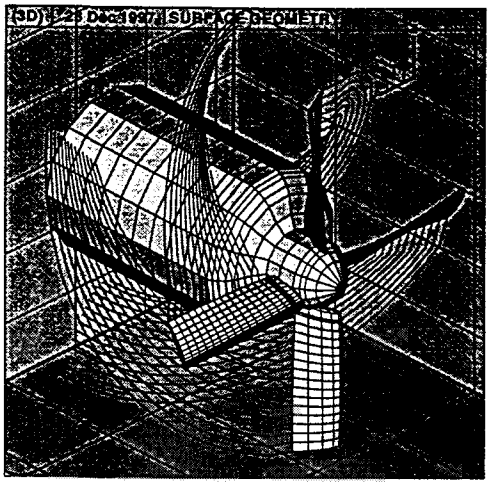

Fig. 4 The three-dimensional model of the propeller and wake system modeled by BETAPROP.

Trajectory Equations

Icing occurs when supercooled water droplets suspended in the atmosphere impinge and freezw on the surface of the propeller blades and the spinner / nacelle assembly. The water droplet diameters of 10 to 50 μm were considered here. These droplets experience a relatively low Reynolds numbers (less than 10^3). Therefore, it can be assumed that the droplets remain spherical in shape. For the low cloud liquid water content (LWC) assumed in the code, it can also be assumed that the droplets do not effect the flow field. A propeller fixed non-inertial reference frame will be used to eliminate the time dependence from the flow field solution. In the rotating reference frame of the code, the propeller's plane of rotation is assumed to be in the $x-z$ plane. As depicted in Fig. 1, the propeller is assumed to be rotating about the y axis with angular velocity vector $\vec{\omega} = [0, \omega, 0]^T$. In a non-inertial reference frame, Newton's second law applied to the droplet motion takes the form:

$$\sum_i \vec{\mathbf{F}}_i = m\left(\ddot{\vec{r}} + 2\vec{\omega} \times \dot{\vec{r}} + \vec{\omega} \times \vec{\omega} \times \vec{r}\right) \qquad (1)$$

where the vector $\vec{r} = [x, y, z]^T$ is the position vector of the droplet with respect to the rotating frame attached to the propeller. The droplet mass m in Eq. (1) is multiplied by the absolute acceleration terms. Performing the time differentiation and the cross products, the absolute acceleration components in Eq. (1) become

$$\frac{d^2(\vec{r})}{dt^2} = \begin{pmatrix} \ddot{x} + 2\omega\dot{z} - \omega^2 x \\ \ddot{y} \\ \ddot{z} - 2\omega\dot{x} - \omega^2 z \end{pmatrix} \qquad (2)$$

The forces acting on the droplet are the gravity force $\vec{G}$, buoyancy force $\vec{B}$ and the drag force $\vec{D}$. The droplet's drag is in the direction of the droplet's *slip velocity* $\vec{V}_{slip} = [V_{s_x}, V_{s_y}, V_{s_z}]^T$ which is the vector difference between the *droplet's velocity* $\vec{U} = [U_x, U_y, U_z]^T$ and the *fluid velocity* $\vec{V} = [v_x, v_y, v_z]^T$ at droplet position $\vec{r}$. The aerodynamic drag force on the droplet calculated in the rotating reference frame is given by

$$\vec{D} = \frac{1}{2}\rho \|\vec{V}_{slip}\| \vec{V}_{slip} A_d C_D \qquad (3)$$

where A_d and C_D are the droplet's cross-sectional area and drag coefficient, respectively. It is assumed that the droplet is a sphere of mass density ρ_d and of diameter d, with mass $m = \rho_d \frac{\pi d^3}{6}$ and cross-sectional area $A_d = \pi \frac{d^2}{4}$. With the magnitude of the slip velocity defined as $V_s = \|\|\vec{V}_{slip}\|\| = \|\vec{V} - \vec{U}\|\|$, the drag force can be expressed as

$$\vec{D} = \pi \frac{d^3}{8} \rho C_D \begin{pmatrix} V_s V_{sx} \\ V_s V_{sy} \\ V_s V_{sz} \end{pmatrix} \qquad (4)$$

Since the gravity and buoyancy forces are stationary with respect to an inertial reference frame, each will appear to be time dependent to an observer rotating with the coordinate system (x, y, z). Given the rotation is about the y axis at a constant angular velocity ω, both forces will have components in the x and z direction only. In vector component form, the buoyancy and gravitational forces are

$$\begin{pmatrix} G_x \\ G_y \\ G_z \end{pmatrix} = \frac{\rho_d \pi d^3}{6} g \begin{bmatrix} -\cos(\omega t) \\ 0 \\ \sin(\omega t) \end{bmatrix} \qquad (5)$$

$$\begin{pmatrix} B_x \\ B_y \\ B_z \end{pmatrix} = g\rho \frac{\pi d^3}{6} \begin{bmatrix} \cos(\omega t) \\ 0 \\ -\sin(\omega t) \end{bmatrix} \qquad (6)$$

Copyright © 1997, American Institute of Aeronautics and Astronautics, Inc.

Summing all the forces and substituting in Eq. (1) we get the following set of differential equations which describe the motion of the droplet as seen from the rotating reference frame:

$$\begin{aligned} \frac{3C_D\sigma V_s V_{sx}}{4d} + g(\sigma-1)\cos(\omega t) &= \ddot{x} + 2\omega\dot{z} - \omega^2 x \\ \frac{3C_D\sigma V_s V_{sy}}{4d} &= \ddot{y} \\ \frac{3C_D\sigma V_s V_{sz}}{4d} + g(1-\sigma)\sin(\omega t) &= \ddot{z} - 2\omega\dot{x} - \omega^2 z \end{aligned} \tag{7}$$

Introducing the *characteristic length* L of the propeller and the *characteristic velocity* U_∞, we define the non-dimensional coordinates (ξ, η, ζ), the non-dimensional angular velocity $\bar{\omega} = \frac{\omega L}{U_\infty}$, dimensionless time $\tau = \frac{tU_\infty}{L}$ and dimensionless slip velocity $\vec{V}_s = (\frac{V_{sx}}{U_\infty}, \frac{V_{sy}}{U_\infty}, \frac{V_{sz}}{U_\infty})$. We define, respectively, the *inertia parameter*, the *freestream Reynolds number* based on the droplet diameter, and the *Froude number* of the flow

$$\begin{aligned} K &\equiv \frac{\rho_d d^2 U_\infty}{18\mu L} \\ R_\infty &\equiv \frac{\rho U_\infty d}{\mu} \\ F_r &\equiv \frac{U_\infty}{\sqrt{L g_0}} \end{aligned}$$

Substitution yields the non-dimensional form of the droplet equation of motion in a rotating reference frame:

$$\begin{aligned} \frac{C_D R_\infty \bar{V}_s}{24K}\bar{V}_{sx} + \frac{1}{F_r^2}\frac{g}{g_0}(\sigma-1)\cos(\bar{\omega}\tau) &= \ddot{\xi} + 2\bar{\omega}\dot{\zeta} - \bar{\omega}^2\xi \\ \frac{C_D R_\infty \bar{V}_s}{24K}\bar{V}_{sy} &= \ddot{\eta} \\ \frac{C_D R_\infty \bar{V}_s}{24K}\bar{V}_{sz} + \frac{1}{F_r^2}\frac{g}{g_0}(1-\sigma)\sin(\bar{\omega}\tau) &= \ddot{\zeta} - 2\bar{\omega}\dot{\xi} - \bar{\omega}^2\zeta \end{aligned} \tag{8}$$

The spherical water droplets experience Reynolds numbers in the range of

$$0 > R_s \leq 1000 \tag{9}$$

For Reynolds number within this range, Langmuir and Blodgett,[8] determined the following expression for the fraction $\frac{C_D R_\infty}{24}$, which is valid for low-speed atmospheric droplets where compressibility effects are negligible

$$\left(\frac{C_D R_s}{24}\right) = 1.0 + 0.197 R_s^{0.63} + 2.6\times10^{-4} R_s^{1.38} \tag{10}$$

where the *slip velocity Reynolds number* is defined by

$$R_s \equiv \frac{\rho V_s d}{\mu} = R_\infty V_s \tag{11}$$

Equations (8) contain two similarity parameters K and R_∞ that characterize the particle's motion in the flow field around a given body of characteristic dimension L. It is possible to combine the inertia parameter K and the freestream Reynolds number R_∞ into a single similarity parameter K_0, called the *modified inertia parameter* by defining K_0 as

$$K_0 \equiv \frac{K}{R_\infty}\int_0^{R_\infty} \frac{1}{\left(\frac{C_D R_\infty}{24}\right)} dR_\infty \tag{12}$$

The integral in the equation above was first evaluated by Bragg[9] and can be expressed in the following relation

$$K_0 = 18K\left[R_\infty^{-\frac{2}{3}} - \sqrt{6}R_\infty^{-1}\arctan\left(\frac{R_\infty^{\frac{1}{3}}}{\sqrt{6}}\right)\right] \tag{13}$$

In aircraft icing research, forces experienced by the droplets due to gravity and buoyancy are orders of magnitude smaller than the drag force on the droplets. It is therefore customary to neglect the effects of gravity and buoyancy in the equations of motion of the water droplets. This is a practical assumption for the size and mass of droplets often encountered in atmospheric icing clouds. Defining $\varphi(R_s) = \frac{C_D R_s}{24}$, and introducing the state variables $(X_1, X_2, \ldots, X_6) = (\xi, \dot{\xi}, \eta, \dot{\eta}, \zeta, \dot{\zeta})$ The equations of motion of the droplet can be written as the six first-order coupled ordinary differential equations:

$$\begin{aligned} \dot{X}_1 &= X_2 \\ \dot{X}_2 &= \frac{\varphi(R_s)}{K}\left(\frac{U_x}{U_\infty} - X_2\right) - 2\bar{\omega}X_6 + \bar{\omega}^2 X_1 \\ \dot{X}_3 &= X_4 \\ \dot{X}_4 &= \frac{\varphi(R_s)}{K}\left(\frac{U_y}{U_\infty} - X_4\right) \\ \dot{X}_5 &= X_6 \\ \dot{X}_6 &= \frac{\varphi(R_s)}{K}\left(\frac{U_z}{U_\infty} - X_6\right) + 2\bar{\omega}X_2 + \bar{\omega}^2 X_5 \end{aligned} \tag{14}$$

Copyright © 1997, American Institute of Aeronautics and Astronautics, Inc.

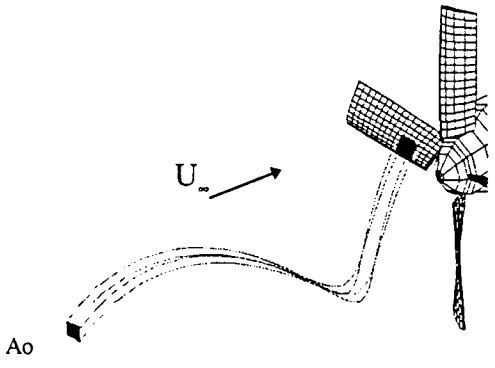

Fig. 5 Local impingement efficiency on a 3D surface.

The state space equations above are numerically integrated with respect to time. Only initial conditions are required to start the numerical integration. It is assumed that the droplet starts at rest with respect to the freestream velocity vector as seen from the rotating reference frame. Therefore, a droplet far upstream will appear to an observer on the rotating propeller to have velocity components that depend on the z and x coordinates of the droplet initial position in space. The axial velocity component, however, will be the freestream velocity in the negative y direction.

A point Q far upstream from the propeller with the non-dimensional coordinates coordinates $\vec{R}_Q = (\xi, \eta, \zeta)$ at time $\tau = 0$ will have the initial velocity $\vec{V}_Q = -\vec{\omega}_Q \times \vec{R}_Q$. Performing the vector cross product and combining the result with the initial axial velocity, the initial velocity at point Q can be expressed as

$$\vec{V}_Q = \begin{bmatrix} (-\bar{\omega}\zeta)\,\vec{i} \\ (\bar{V}_\infty)\,\vec{j} \\ (\bar{\omega}\xi)\,\vec{k} \end{bmatrix} \tag{15}$$

Local Emingement Efficiency β

The local collection efficiency of the surface is defined in three dimensions as the ratio of the cross-sectional area of the mass tube far upstream of the body to the surface area of the body bounded by the impinging stream tube, i.e., Fig. 5.

Assuming that the droplets are at rest with respect to freestream, the four trajectories impinging on the corner points of a surface panel covering the area where the β value is desired are found by iteration on the initial conditions. The upstream cross-sectional area of the bounding stream tube A_0 and the panel surface area A_S are respectively calculated. Note that A_0 is normal to the freestream. The average local collection efficiency is then computed by:

$$\beta = \frac{A_0}{A_S} \tag{16}$$

Total Collection Efficiency E

The total collection efficiency on a given radial segment of the propeller that has been approximated by a set of N flat surface panels is defined by

$$E_{3D} = \frac{1}{A_p} \int_{(\frac{s}{c})_L}^{(\frac{s}{c})_U} \beta \; d(A) \tag{17}$$

where A_p is the projected area of the segment of the blade under consideration. In this 3D analysis, A_p will be taken as the projected frontal area of the propeller segment as seen from the axial direction. The total collection efficiency will then be noted as E_{3D}. In two-dimensional icing analysis, the expression for E takes a similar form. The surface integral in Eq. (17) is replaced by a line integral evaluated over the surface of the airfoil and A_p is replaced by the projected height of the airfoil section taken perpendicular to the local relative velocity vector. The resulting two-dimensional total collection shall be referred to as E_{2D}.

CODE VALIDATION

The code was used to model a 36 inch diameter propeller blade rotating at 500 RPM. The freestream velocity was $40.0\frac{ft}{s}$. The corresponding advance ration was $J = 1.6$. The 4.5-inch chord propeller blade was assumed to have a constant Clark-Y airfoil section. The blade cross-section is tapered in to a 1.25 inch diameter cylinder at the root. The tapering starts from 18.05% station and continues to the base of the blade. The blade was linearly twisted with $\beta_{75\%} = 39.35°$.

To validate the code, the propeller blade above was modeled as a single blade without a spinner or nacelle. This was done in order to compare the performance results of each 3D solution to the two-dimensional results uncorrected for the effects of multiple blades and center body / nacelle blockage.

Copyright © 1997, American Institute of Aeronautics and Astronautics, Inc.

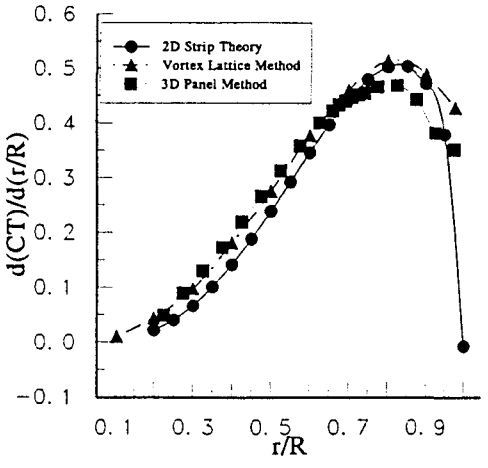

Fig. 6 Radial thrust distribution.

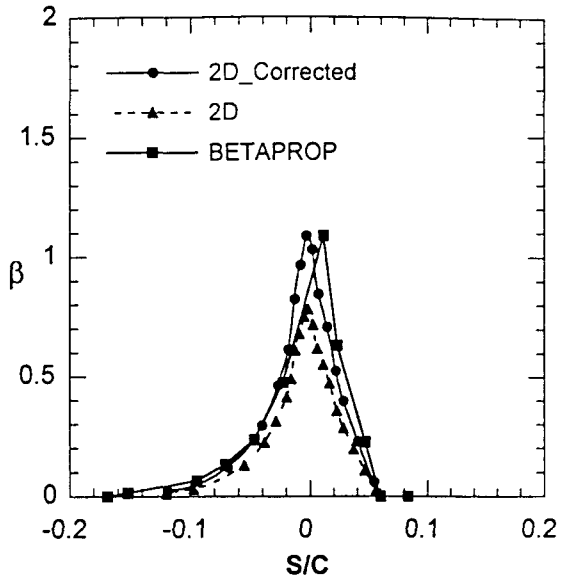

Fig. 7 BETAPROP compared to the $\beta_{2D_{corrected}}$ for a two-bladed propeller with J=2.0, $d = 20\mu m, \frac{r}{R} = 0.50$

The flow fields were determined from the VLM and PM modules of the code. In both cases, the resulting lift force was resolved in the thrust direction and the radial distribution of thrust was determined. In Fig. 6 the radial thrust distribution as calculated by the VLM , PM and the 2D strip theory results calculated by the Lan and Roskam[10] method or that outlined by McCormick[11]. With the exception of the tip region, both solutions predict similar thrust characteristics. The 3D panel solution predict a 10% lower thrust than the 2D strip theory and the VLM. This is attributed to the ability of the PM to model the tip losses more accurately than the other two methods.

Comparison to 2-D Data

By writing a conservation of mass expression for the liquid water impinging on the surface of the blade to that crossing a stream tube perpendicular to the effective velocity vector, and further nondimensionalizing by the freestream mass flux, it can readily be shown that β_{2D} and $\beta_{2D_{corrected}}$ are related by the expression:

$$\beta_{2D_{corrected}} = \beta_{2D}\mathcal{F}(J, \frac{r}{R}) \qquad (18)$$

where $\mathcal{F}$ is a function defined by:

$$\mathcal{F}(J, \frac{r}{R}) = \left[1 + \left(\frac{\pi\left(\frac{r}{R}\right)}{J}\right)\right]^{1/2} \qquad (19)$$

Equation (18) implies that $\beta_{2D_{corrected}} \geq \beta_{2D}$. The factor $\mathcal{F}(J, \frac{r}{R})$ defined by Eq. (19) accounts for the increase in liquid mass impingement due to the rotation of the propeller.

In Fig.7, the BETAPROP code results for $\frac{r}{R}$ = 50% radial location on a two-blade propeller are compared to the β_{2D} and $\beta_{2D_{corrected}}$. It is important to note that values for β_{2D} appearing in the right hand side of Eq. (18) are calculated by Bragg's AIRDROP[12] code. β_{2D} was computed for the Clark-Y airfoil operating at the same lift coefficient. The droplet inertia parameter and Reynolds number used to calculate the β_{2D} curve were found using the airfoil chord and effective velocity as the characteristic length and velocity, respectively.

Consistently, the BETAPROP curves closely resemble the $\beta_{2D_{corrected}}$ curves which to a certain degree validates the relationship in Eq. (18) and the BETAPROP code. Although both methods predict the same upper limits of impingement, the three-dimensional approach predicts the lower limits of impingement closer to the trailing edge. $\beta_{3D_{max}}$ consistently was predicted on the upper surface corresponding to $\frac{S}{C} = +.015$.

Comparison to 3-D Experimental Data

In order to experimentally validate the BETAPROP code, the droplet impingement on a four-bladed wind tunnel propeller model was experimentally measured by Riechhold.[13] The propeller model and the tunnel settings were selected to be representative of a commuter turbo-prop at cruise conditions. The 36-inch diameter four-bladed propeller

Copyright © 1997, American Institute of Aeronautics and Astronautics, Inc.

was tested in the UIUC wind tunnel which was fitted with five NASA standard spray nozzles. Thin strips of chromatography paper were placed on the propeller surface at the 25%, 35%, 50%, 70% and 90% radial locations. Dye laden water was injected into the tunnel via the spray system for a given spray time. The new dye-tracer technique developed by Bragg et al.[14] was then used to determine the collection efficiency on the propeller blade.

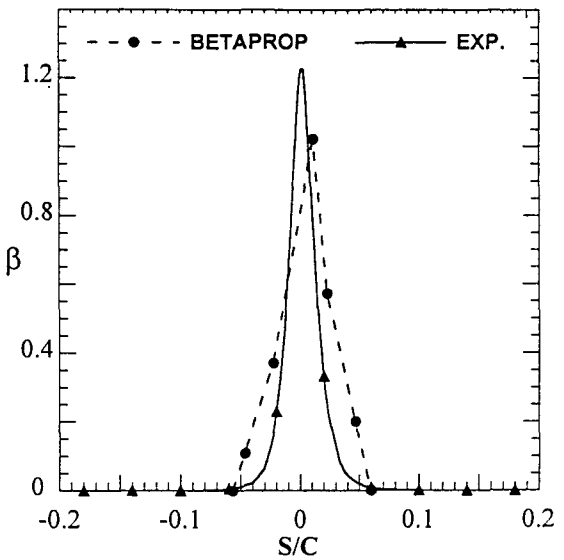

Fig. 8 Impingement efficiency for the baseline configuration, $\frac{r}{R} = 0.50$, $d = 15\mu m$, $K_0 = .006$, $J = 1.6$

The *baseline propeller* test configuration was a four-bladed propeller with $\beta_{75\%} = 40°$ together with an axi-symmetric engine nacelle 10 inches in diameter. The propeller impingement experiments were performed in $15\mu m$, $20\mu m$, and $30\mu m$ MVD spray clouds. Additional experiments were conducted using a 16-inch axi-symmetric nacelle in two-and four-blade configurations.

The experimental and computational β_{3D} results at $\frac{r}{R} = 50\%$ for the MVD values of 15, 20 and $30\mu m$ (the baseline configuration) are shown in Fig. 8, 9, and 10, respectively. Figure 11 displays results at the same radial location corresponding to the large nacelle case. The experimental data generally were in agreement with the trends predicted by the BETAPROP code. The 3D code predicted the experimental upper limits of impingement well. Consistently however, the experimental β_{max} values were larger than the predicted 3D values. The difference in β_{max} was as high as 35% as in Fig. 9. For the large nacelle cases however, the differences in the β_{max} values did not exceed 15% at every radial station. The impingement efficiencies calculated by BETAPROP for the 16-inch nacelle case were in better agreement with the experimental data than for the calculations for the 10-inch nacelle case.

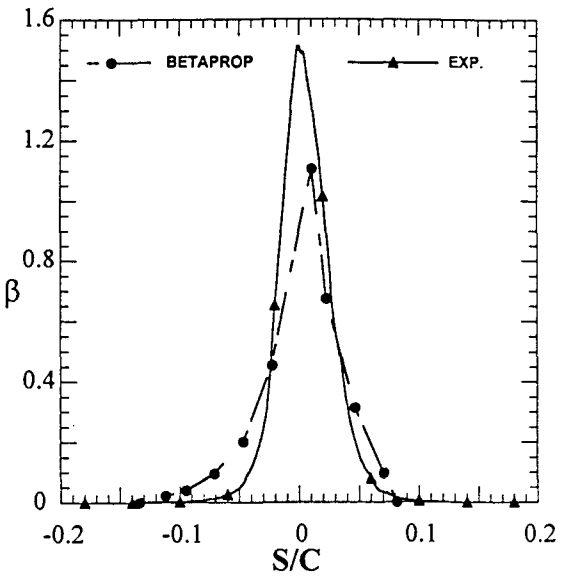

Fig. 9 Impingement efficiency for the baseline configuration, $\frac{r}{R} = 0.50$, $d = 20\mu m$, $K_0 = .01$, $J = 1.6$

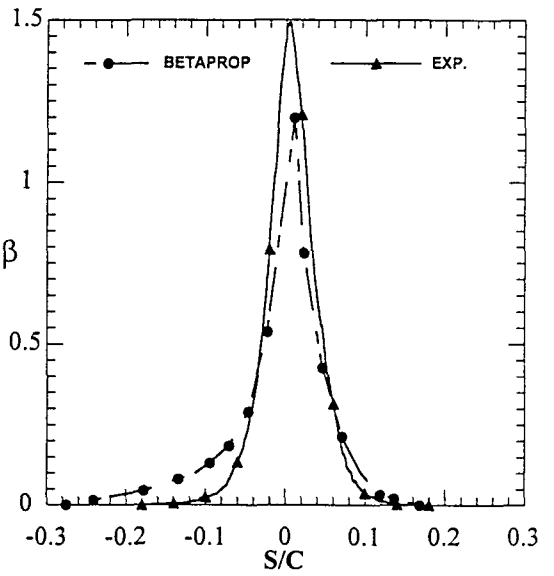

Fig. 10 Impingement efficiency for the baseline configuration, $\frac{r}{R} = 0.50$, $d = 30\mu m$, $K_0 = .02$, $J = 1.6$

The code generally predicted the lower impingement limits to be closer to the trailing edge. For the large nacelle configuration, the computational β_{3D} curves in Figs. 11, 12 and 13 indicated that more mass was collected on the lower blade surface. The

Copyright © 1997, American Institute of Aeronautics and Astronautics, Inc.

experimental results do not show such trends.

It is important to note that the calculated uncertainties for this experimental technique of Bragg et al.[14] is 15.44%. The uncertainties are primarily due to the uncertainty in the spray cloud MVD and variations in the ambient conditions of the different clouds tested in the tunnel. The uncertainty in the experimental impingement efficiency values were calculated by Reichhold[13] using in part the measured standard deviation in the mass of the dye collected on the freestream collector, the standard deviation in the propeller data and that of the corresponding collector at each radial location. The uncertainty in the experimental impingement efficiencies were reported to be less than or equal 16% at β_{max}. The uncertainty increase as the impingement limits were approached to 30% – 50% of the local β.

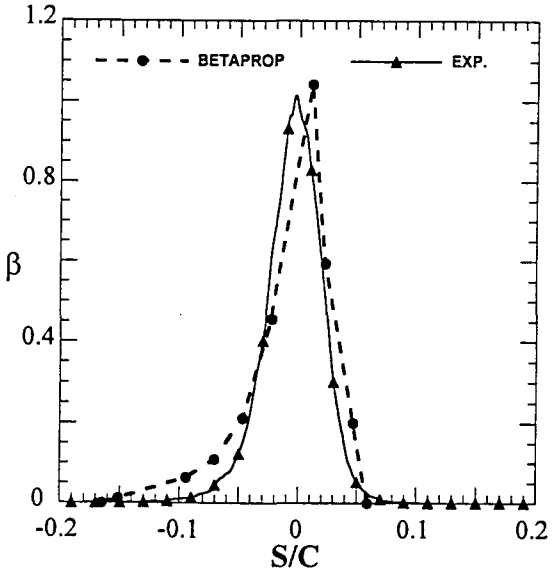

Fig. 11 Impingement efficiency for the large nacelle configuration, $\frac{r}{R} = 0.50$, $d = 20\mu m$, $K_0 = .01$, $J = 1.6$

In an attempt to remove some of the uncertainty in the experimental data for the purpose of comparison, the experimental impingement efficiency curves were normalized by β_{max} and compared to their computational counterparts in Figs. 14-17. Comparison of the normalized beta curves exhibit differences between the experimental data and those from the BETAPROP code. The difference could be due in part to the uncertainty in the experimental data. The tendency for codes to over predict the experimental β value near the limits of impingement

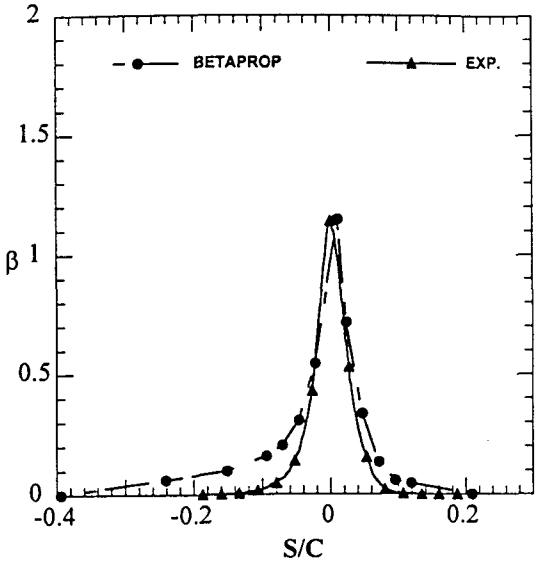

Fig. 12 Impingement efficiency for the large nacelle configuration, $\frac{r}{R} = 0.50$, $d = 30\mu m$, $K_0 = .02$, $J = 1.6$

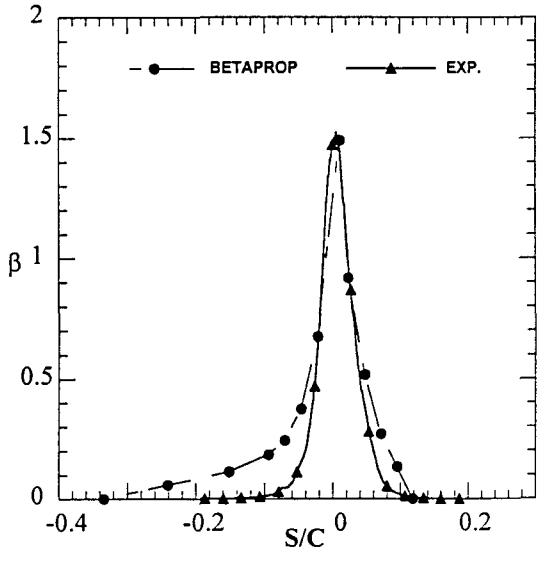

Fig. 13 Impingement efficiency for the large nacelle configuration, $\frac{r}{R} = 0.70$, $d = 30\mu m$, $K_0 = .02$, $J = 1.6$

Copyright © 1997, American Institute of Aeronautics and Astronautics, Inc.

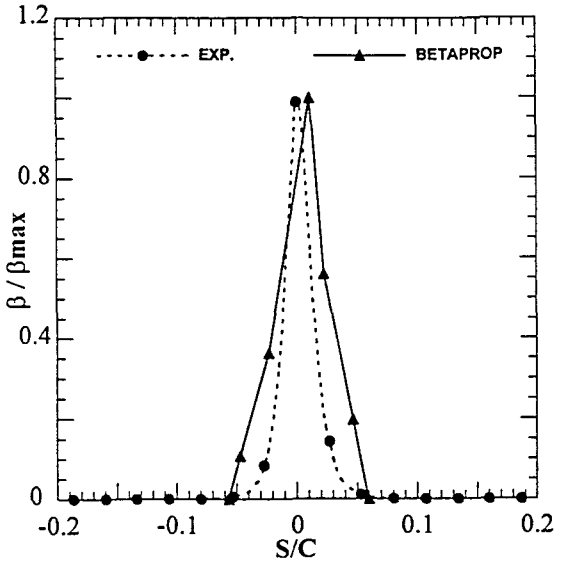

Fig. 14 β/β_{max} for the baseline configuration, $\frac{r}{R}$ = 0.50, $MVD = 15\mu m$, $K_0 = .006$, $J = 1.6$

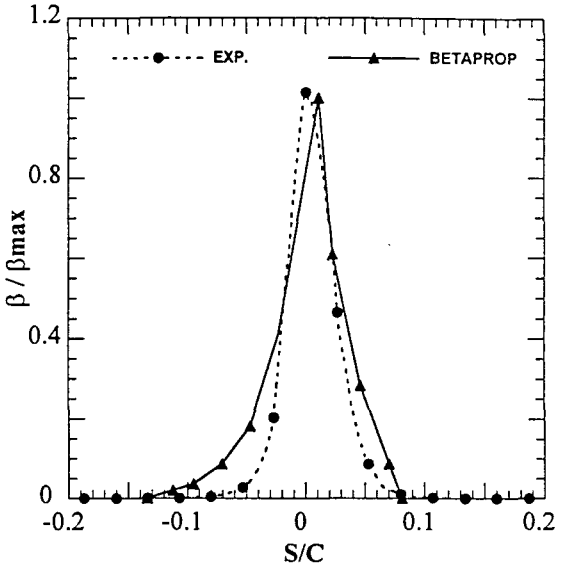

Fig. 15 β/β_{max} for the baseline configuration, $\frac{r}{R}$ = 0.50, $MVD = 20\mu m$, $K_0 = .01$, $J = 1.6$

is very similar to that seen in the two-dimensional comparisons to the experimental work done by Papadakis et al.[15]

Based on the agreement of the BETAPROP code results $\beta_{2D_{corrected}}$ and the general agreement with the trends of the experimental data available at this time, the BETAPROP code can be used with confidence to analyze other three-dimensional propeller/nacelle combinations.

RESULTS AND DISCUSSION

The code has been used in a study to determine the significance of three-dimensional effects on the droplet trajectories in the vicinity of 3D propellers. The radial variation of the impingement efficiency for the baseline configuration with MVD of $15\mu m$, $20\mu m$ and $30\mu m$ are shown in Figs. 18, 19 and 20 respectively.

At very radial location, increasing the droplet size increases β_{max} and causes the lower and upper limits of impingement to move closer to the trailing edge. In Fig. 18, the 70% station of the baseline case was examined. Changing the droplet size from 15μ to 30μ caused a 13% increase in β_{max}. The lower and upper impingement limits also increased by 80% and 55%, respectively.

With the propeller rotation rate held constant at 500 RPM, the number of blades was reduced from the baseline four-blade configuration to two blades.

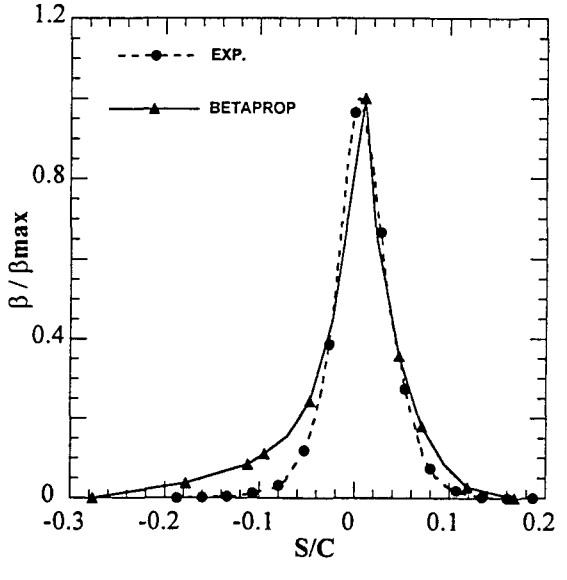

Fig. 16 β/β_{max} for the baseline configuration, $\frac{r}{R}$ = 0.50, $MVD = 30\mu m$, $K_0 = .02$, $J = 1.6$

Copyright © 1997, American Institute of Aeronautics and Astronautics, Inc.

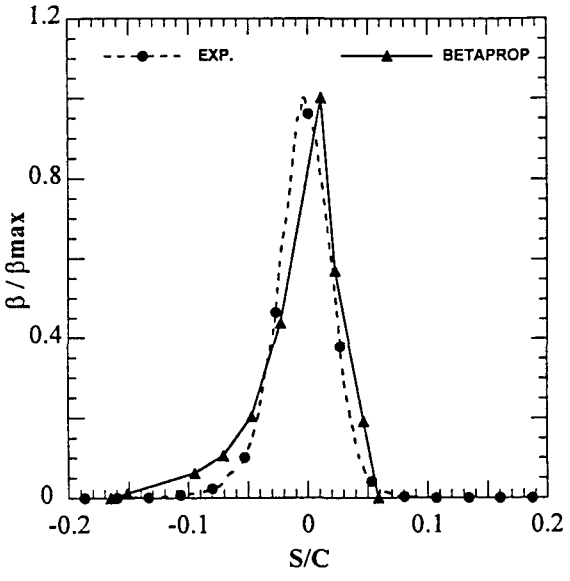

Fig. 17 β/β_{max} for the large nacelle configuration, $\frac{r}{R} = 0.50$, $MVD = 20\mu m$, $K_0 = .01$, $J = 1.6$

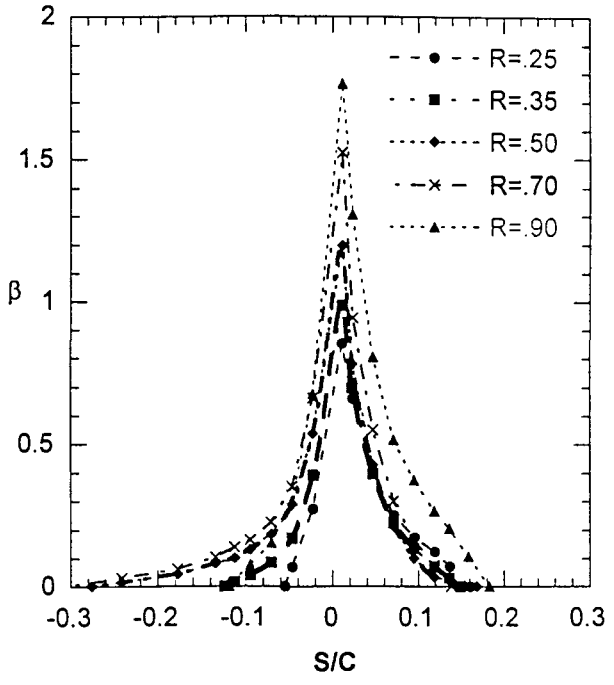

Fig. 19 Impingement efficiency for the baseline configuration $d = 20\mu m$, $K_0 = .01$, $J = 1.6$

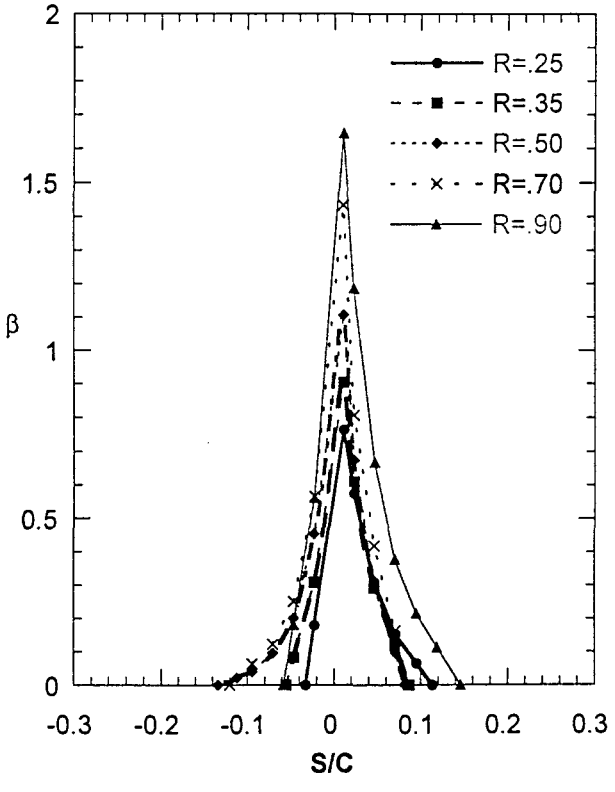

Fig. 18 Impingement efficiency for the baseline configuration $d = 15\mu m$, $K_0 = .006$, $J = 1.6$

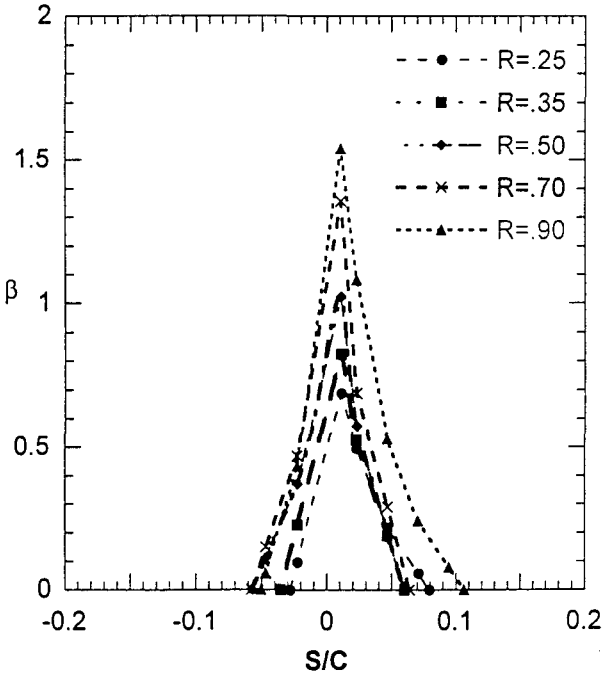

Fig. 20 Impingement efficiency for the baseline configuration $d = 30\mu m$, $K_0 = .02$, $J = 1.6$

Copyright © 1997, American Institute of Aeronautics and Astronautics, Inc.

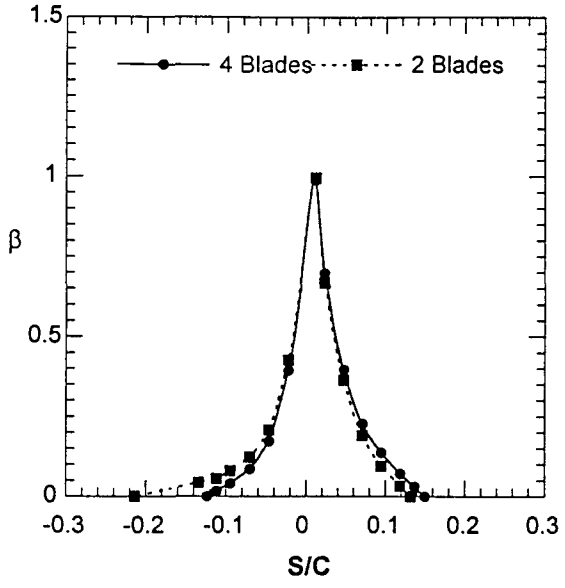

Fig. 21 Impingement efficiency of two propellers, $r/R = 0.35$, $d = 30\mu m$, $K_0 = .0210$, $J = 1.6$, 10" diameter nacelle.

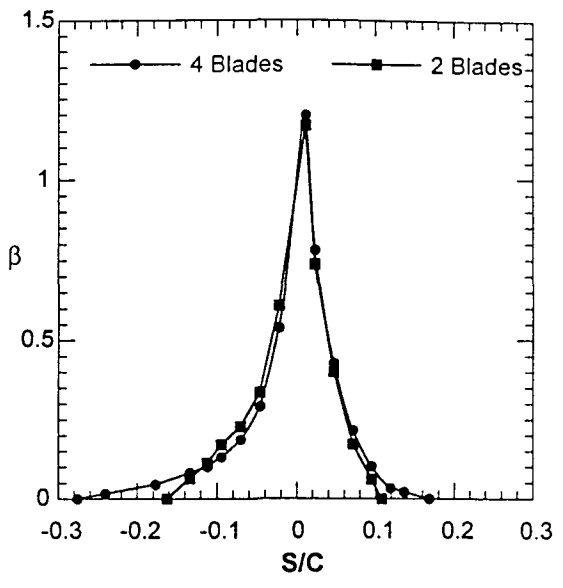

Fig. 22 Impingement efficiency of two propellers, $r/R = 0.50$, $d = 30\mu m$, $K_0 = .0210$, $J = 1.6$, 10" diameter nacelle.

It was observed that such reduction of the number of blades had essentially no effect on the icing characteristics near the root and tip of the blade. At the 35% radial location, Fig. 21, the lower limit of impingement was slightly displaced further back towards the trailing edge. The rest of the β curve and the upper limit of impingement remained essentially unchanged.

Only at the mid-span of the blade, Fig. 22, did the lower and upper limits of impingement move towards the stagnation point. The maximum effects of the reduction of the number of blades occurred at the 50% radial location. The movement of the impingement limits decreased in magnitude at the 70% radial location to completely vanish at the 90% radial location. For the same power settings, varying the number of blades had no influence on β_{max} nor $(S/C)_{\beta_{max}}$.

To achieve optimum propulsive efficiency, typical turboprop must operate over a wide range of advance ratio J. In take off and landing configurations, characterized by low flight velocities, constant speed propellers are set at high rotational rates; 2200 – 2500 RPM; and low pitch, hence low J settings. When higher flight velocities are reached at cruise configuration, propeller RPM is usually set in the range of 1800 – 2200 RPM and the propeller pitch is varied (Via the governer) to maintain constant rotational speed.

The icing characteristics of propellers greatly depend on the propeller power settings. In Fig. 23, the local impingement efficiency at the 50% radial location of the propeller is plotted for different advance ratio J. In each case, the blade pitch was varied to match the same local lift coefficient $C_l = 0.717$, and hence a fixed local effective angle of attack, $\alpha_{eff} = 2.34°$. For the graphs in Fig. 23, the values of the 2D and 3D modified inertia parameters and the rotation correction factor, Eq. (19), are listed in table 1.

It is evident that at low J values resulting from low U_∞, the propeller experiences substantial in-

J	U_∞	U_{rel}	K_0	$K_{0_{2D}}$	$\mathcal{F}$
0.8	20	44.06	.0059	.0889	2.230
1.2	30	49.41	.0082	.0970	1.647
1.6	40	56.05	.0103	.1066	1.401
2.0	50	63.57	.0122	.1170	1.272
2.4	75	89.63	.0165	.1496	1.195

Table 1 The variation of icing parameters with advance ratio J, $\frac{r}{R} = 0.5$, $d = 20\mu m$.

Copyright © 1997, American Institute of Aeronautics and Astronautics, Inc.

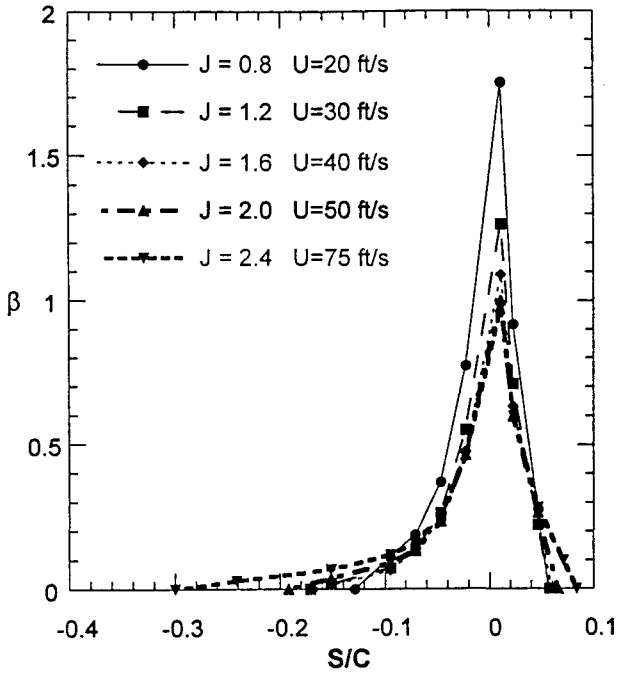

Fig. 23 Icing characteristics of two bladed propellers with a variable J, $r/R = 0.50$, $d = 20\mu m$, $C_l = .717$

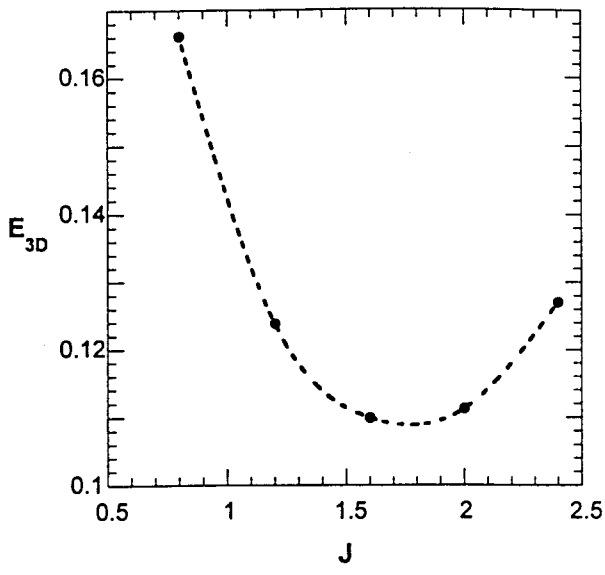

Fig. 24 Total collection for a two bladed propeller configuration at $r/R = 0.50$, $d = 20\mu m$, $C_l = .717$

crease in β_{max} along the leading edge of the blade. This occurred despite the fact that K_0 and $K_{0_{2D}}$ increased with increasing J. This can be explained by noting that with the rotation rate held constant, the blade with a low J setting have experienced more rotations within a given translation distance forward, than a blade at a higher J setting. Therefore, the propeller blade with the low J setting would sweep a larger volume.

As the axial flow velocity increases, the propeller completes fewer rotations as it advances forward an equal distance, hence a stream tube of less volume will be swept by the blade segment. Although the upper limit of impingement remains relatively unaffected by variations in J, the lower limit of impingement moves farther from the stagnation point as J increases. The movement of the lower limit towards the trailing is the result of the slight increase in the magnitude of the effective velocity vector. Droplets approaching the blade with the larger effective velocity have higher K_0 values. Given that C_l is constant, the lower limits of impingement move further back on the lower surface.

The graphs in Fig. 23 show the total collection to be dependent on the advance ratio. Integrating all the distributions according to Eq. (17), the resulting E_{3D} values are plotted in Fig. 24 as a function of J. It is noted that such dependence is nonlinear. Figure 24 shows the collection reaches a minimum at $J = 1.75$. With the RPM held constant, operating the propeller at $J < 1.75$ increases the total collection due to the rotational effects described earlier. If $J > 1.75$, the effects of high K_0 values dominate and cause E_{3D} to increase.

The blockage effects of the nacelle on the impingement characteristics of the propeller blade have been considered. Figures 25 and 26 show the β distribution at the 50% and 70% radial locations of the baseline configuration, respectively. For comparison, the impingement efficiencies for the 16-inch and 22-inch nacelle cases are also depicted on the same graph. In addition, the β distribution for the *No Nacelle* (spinner only) geometry as well as the β_{2D} distribution corrected for rotational effects via Eq. (18) have been plotted. It is noted that the 10" diameter nacelle corresponds to 7.71% area blockage of the flow through the 36" diameter propeller disc. The 16-and 22-inch diameter nacelles correspond to 19.75% and 37.35% area blockage, respectively.

Increasing the nacelle diameter causes substantial movement of the lower limit of impingement towards the trailing edge. A trend of lesser magnitude was also present on the upper limit of impingement. The upper impingement limit shifted towards the stagnation point with increasing nacelle diameter. β_{max} decreased by less than 10% as the nacelle diameter was varied over the range of 10 - 22 inches. The movement of the lower limit of impingement

Copyright © 1997, American Institute of Aeronautics and Astronautics, Inc.

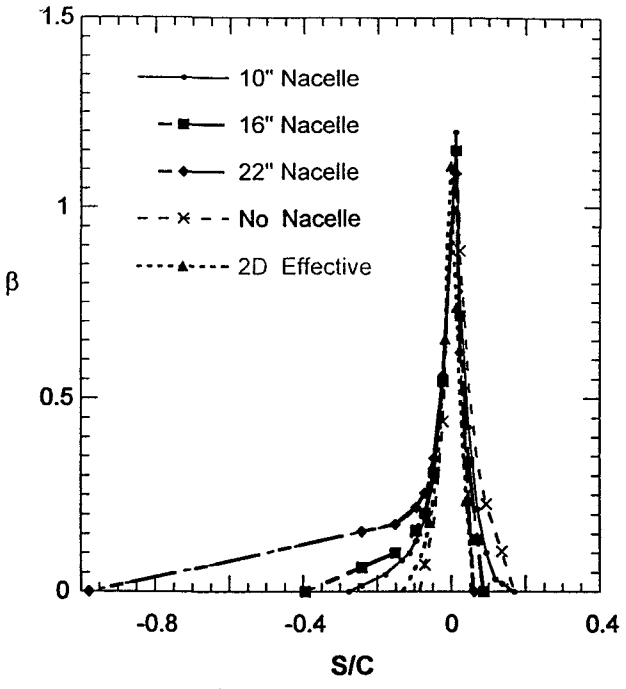

Fig. 25 Propeller with varying nacelle configurations. $r/R = 0.50$, $d = 30\mu m$, $J = 1.6$

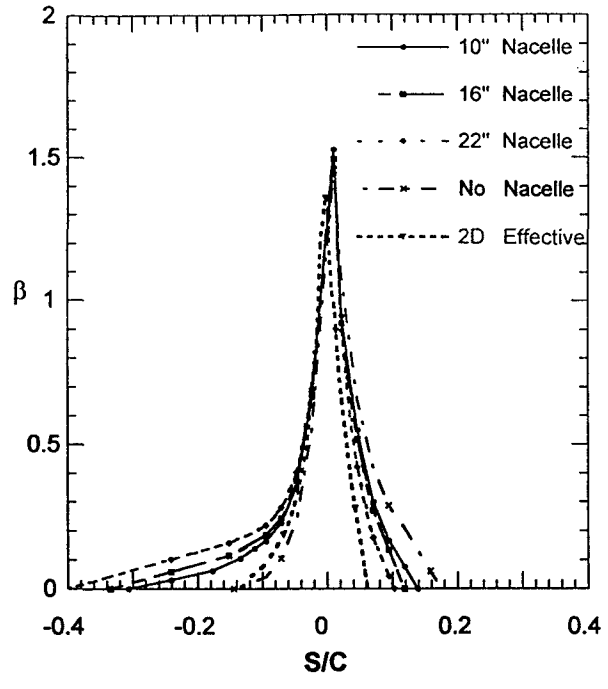

Fig. 26 Propeller with varying nacelle configurations. $r/R = 0.70$, $d = 30\mu m$, $J = 1.6$

towards the trailing edge correspond to an increase in the angle of attack. This is caused by the reduction in axial velocity caused by the nacelle. It is important to realize that significant changes in the impingement characteristics of the blade have emerged due to the three-dimensional aerodynamic blockage caused by the nacelle. Note that the 2D impingement data corrected for rotational effects, shown in Figs. 25 and 26, underestimate the limits of impingement and the total collection.

For the $20\mu m$ and $30\mu m$ droplet sizes, the effects of the nacelle on the impingement efficiency profiles were insignificant near the root of the blade at the 25% radial location. The effects of the nacelle blockage for these two droplet sizes begin to appear starting at the 35% radial location. The nacelle effects on the 20 and 30 μm droplet sizes reach maximum at the 50% radial location. The nacelle blockage effects on the $20\mu m$ and $15\mu m$ particles start to decrease from the 50% radial location until they virtually vanish at the 90% radial location. Droplets with moderate inertia experience significant radial acceleration due to the axi-symmetric flow about the spinner and nacelle. The outward radial acceleration of the large droplets reduces their impingement at the root of the blade and enhances it at the midspan of the blade. The axi-symmetric spinner and nacelle cause a radial droplet sorting effect along the blade.

The small $15\mu m$ droplets, however, were affected by the nacelle blockage at every radial location on the blade. This greater sensitivity to flow disturbance, caused by the nacelle blockage, is due to the droplets low inertia. The aerodynamic drag of low mass droplets, hence low inertia, tend to make the droplets follow the stream lines of the flow field.

CONCLUSIONS

A droplet trajectory code for propellers, BETAPROP, was described. A three-dimensional vortex lattice method and first-order panel method were used to calculate the invicid incompressible flow. This method allowed the modeling of complex 3D propeller geometries with axi-symmetric nacelles. The droplet equations of motion in a non-inertial reference frame were integrated in the 3D flow. The impinging trajectories were used to calculate the local impingement efficiency, limits of impingement and total collection. The 3D results obtained from the BETAPROP code were compared to 3D experimental data and 2D computational data corrected for rotational effects. Comparison of the 3D code results with the 3D experimental data shows reasonable agreement. When single blades without a center body or nacelle are modeled, the 3D results exhibit very good agreement

Copyright © 1997, American Institute of Aeronautics and Astronautics, Inc.

with the two-dimensional AIRDROP code results corrected for rotational effects. For some moderately loaded propellers with slender spinner/nacelle geometry, the two-dimensional droplet impingement codes, corrected for rotational effects, reasonably predicted the impingement efficiencies and the limits of impingement. The BETAPROP code results indicate that the nacelle/spinner geometry is the most important three-dimensional flow-field factor affecting the impingement efficiency and the limits of impingement on propeller blades.

ACKNOWLEDGMENT

This research was supported in part by BF-Goodrich De-Icing systems. The BETAPROP code described in this paper is the property of BF-Goodrich. The authors would like to thank Mr. Dave Sweet for his significant contributions to this work.

REFERENCES

[1] Korkan, K. D. , Dadone, L. and Shaw, R. J. *Performance Degradation of Propeller/Rotor Systemd due to Rime Ice Accretion.* AIAA Paper Number 82-282, The 20th Aerospace Sciences Meeting, 1982.

[2] Korkan, K. D. , Dadone, L. , and Shaw, R. J. *Performance Degradation of Propeller Systems due to Ice Accretion.* Jornal of Aircraft., Vol. 21 No. 1 January, 1984.

[3] Millere, T. L. , Korkan, K. D. , Shaw, R. J. *Analytical Determination of Propeller Performance Degradation due to Ice Accretion.* AIAA paper Number 85-0339, The 23rd AIAA Aerospace Sciences Meeting, 1985.

[4] Korkan, K. D., Dadone, and Shaw, R. J. *Performance Degradation of Helicopters due to Icing - A review.* Paper Presented at the 41st Annual American Helicopter Society Forum and Technology Disply, Fort Worth, Texas, May 15-17, 1985.

[5] Hedde, T. and Guffond, D. *Development of Three-Dimensional Icing Code, Comparison with Experimental Shapes.* AIAA paper Number 92-0041, The 30th Aerospace Sciences Meeting, Reno NV, January, 1992.

[6] Guffond, D. *Prediction of Ice Accretion: Comparison Between 2D and 3D Codes.* Presentation to SAE Subcommittee AC-9C. Meeting No. 21, Aircraft Icing Technology. Toulouse France, September 27-30, 1994.

[7] Ashby, D. L., Dudley, M. R., and Iguchi S. K. *Development and Validation of an Advanced Low-Order Panel Method.* NASA TM 101024, October, 1988.

[8] Langmuir, I. and Blodgett, K. *A Mathematical Investigation of Droplet Trajectories.* In collected works of Irving Langmuir. New York: Pergamon Press, pp 348-393, 1946.

[9] Bragg, M.B. *A similarity Analysis of the Droplet Trajectory Equation.* The AIAA Journal, Volume 20, Number 12, Page 1681, December, 1982.

[10] Lan, C. E. and Roskam, Jan. *Airplane Aerodynamics and Performance.* Roskam Aviation and Engineering Corporation, Ottawa, Kansas, 2nd edition, chapter 7, 1988.

[11] McCormick, B. W. *Aerodynamics, aeronautics and flight Mechanics.* John Wiely & Sons, Inc., 2nd edition, Chapter 6, 1995.

[12] Bragg, M. B. *Rime Ice Accretion and Its Effects on Airfoil performance.* Ph.D. Dissertation, The Ohio State University, Columbus, Ohio, 1981.

[13] Reichhold, J. D. *Experimental Determination of the Droplet Impingement on a Propeller Using a Modified Dye-Tracer Technique.* Master Thesis, Aeronautical And Astronautical Engineering, The University of Illinois at Urbana-Champaign, January, 1997.

[14] Bragg, M. B., Cebrzynski, M. Reichhold, J. D., Sweet, D., Waples, T., and Shick, R. *An Experimental Method for Water Droplet Impingement Measurement.* American Helicopter Society/Society of Automotive Engineers International Icing Symposium, Montreal, Canada, September 18-21, 1995.

[15] Papadakis. M., Elangovan, R., Freund Jr., G. A., Breer, M., Zumwalt, G. W. and Whitmer, L. *An Experimental Method for Measuring Water Droplet Impingement Efficiency on Two- and Three-Dimensional Bodies.* NASA Contractor Report 4257, November, 1989.